



Experimental study of the influence of the rows of vortex generators on turbulence structure in a tube

A. Mokrani, C. Castelain, H. Peerhossaini

► To cite this version:

A. Mokrani, C. Castelain, H. Peerhossaini. Experimental study of the influence of the rows of vortex generators on turbulence structure in a tube. Chemical Engineering and Processing: Process Intensification, 2009, 48 (2), pp.659. 10.1016/j.cep.2008.07.009 . hal-00432288

HAL Id: hal-00432288

<https://hal.science/hal-00432288>

Submitted on 9 Feb 2023

HAL is a multi-disciplinary open access archive for the deposit and dissemination of scientific research documents, whether they are published or not. The documents may come from teaching and research institutions in France or abroad, or from public or private research centers.

L'archive ouverte pluridisciplinaire **HAL**, est destinée au dépôt et à la diffusion de documents scientifiques de niveau recherche, publiés ou non, émanant des établissements d'enseignement et de recherche français ou étrangers, des laboratoires publics ou privés.

***Experimental study of the influence of the
rows of vortex generators on turbulence
structure in a tube***

A. MOKRANI, C. CASTELAIN, H. PEERHOSSAINI*

Thermofluids, Complex Flows and Energy Research Group

Laboratoire de Thermocinétique, UMR CNRS 6607

Polytech Nantes, Rue Christian Pauc,

B.P. 90604

F-44306 NANTES Cedex 3, France

Tél. : +33 2 40 68 31 47

Fax : +33 2 40 68 31 41

- *Corresponding author ; e-mail : cathy.castelain@univ-nantes.fr*

1. Abstract

An experimental study was carried out on the effects of a cascade of longitudinal vortices on the turbulence structure of the flow inside a tube equipped with seven rows of vortex generators. This mixing process is tested in order to be used as a chemical reactor. LIF visualizations of the flow structures show their role in the radial transport mechanism. Measurements of the mean velocity and turbulence quantities were carried out by LDV. The mechanism of radial transfer induce a deformation "in double U" of the axial velocity profile.

The study of the axial velocity fluctuation rate showed that the rows increase notably turbulence in the flow. There is a turbulent flow establishment length, equivalent to the first three rows lines. Besides the axial velocity fluctuation rate does not seem to be sensitive to the Reynolds number, in the studied range. In order to solve the difficulties related to the measurement of the space-time correlations velocity, the fluctuations macro-scale length has been evaluated starting from a relation similar to that obtained by Taylor. A temporal macro-scale, and a suitable convection velocity scale, which take into account the turbulence heterogeneity generated in the static mixer, have been defined. The turbulence dissipation rate was defined based on the Batchelor non-dimensional assumption and the local isotropy of the high frequency fluctuations assumption. It is heterogeneous through the flow cross-section. The hydrodynamic structures generated by the rows increase considerably the turbulence level but they do not diffuse turbulence in the radial flow direction. The Reynolds number does not have a qualitative influence on the turbulence dissipation rate distribution in the studied range. The knowledge of this turbulence characteristic is of a great utility for the prediction of the selectivity of fast chemical reactions.

List of Symbols

C	: Constant
D	: Dispersion coefficient
L	: Mixer length
l_e	: Length scale of the largest eddies in the equilibrium range of the power spectrum
p	: Static pressure
q	: Turbulence kinetic energy
Re	Reynolds number
r	: Radial coordinate
Sc	: Schmidt Number
T	: Integral time scale
T_u	: Turbulence intensity of the velocity U
t	: Time
τ_d	: Characteristic time for vorticity diffusion
τ_m	: Characteristic time for momentum diffusion
$\overline{U}, \overline{V}, \overline{W}$: axial, tangential and radial components of the mean velocity
U_{conv}	: Convection velocity
u, v, w	: Fluctuations of the axial, tangential and radial velocity components
u', v', w'	: RMS of the velocity fluctuations (equivalent to $\sqrt{u^2}$, $\sqrt{v^2}$, $\sqrt{w^2}$)
x, y, z	: Cartesian coordinates
x_o	: Spatial coordinate

Greek symbols

α	: Constant wave length of hairpin vortices separation..
----------	---

λ	: Kolmogorov's micro scale
ε	: Turbulent energy dissipation rate
Λ	: Integral macro length scale of the fluctuations
ν	: Kinematic viscosity
ρ	: Density
$\rho(x_o, \tau)$: Temporal autocorrelation coefficient of axial velocity
σ	: Macro time scale of the fluctuations

2. Introduction

The design of high-efficiency reactors that combine good mixing with efficient heat transfer is important in chemical engineering process intensification. In numerous fields, high turbulence rates and high shearing are rather required. It is the case, especially, in rapid chemical reaction processes. The micromixing becomes then a determining parameter for the selectivity of these reactions. The micro-mixing characteristic size is linked with the Kolmogorov's micro-scale or the energy dissipation rate of turbulence (Baldyga & Bourne [1]). The distribution of the turbulence energy dissipation rate in the flow therefore determines the micro-mixing characteristic size. The mixing speed is also a leading parameter for certain reactions; it is important that the mixing process is finished before that the reactants start to react.

The local energy dissipation rate is the turbulence parameter with the most direct relation to reaction progress and selectivity (see for example Baldyga & Bourne [1]). For this reason, several hydrodynamic studies of mixer-reactors over the last 20 years have focused on predicting or measuring the distribution of this parameter. However, since mechanical stirring

is still widely used in the chemical processing industry, almost all hydrodynamic studies performed to date on mixer-reactors have been based on this type of device (Cutter [2], Sato *et al.* [3, 4], Mujumdar *et al.* [5], Rao & Brodkey [6], Komasaawa *et al.* [7], Gunkel & Weber [8], Okamoto *et al.* [9], Barthole *et al.* [10], Laufhütte & Mersmann [11], Wu & Paterson [12], Baudou *et al.* [13], Mavros *et al.* [14], Michelet *et al.* [15], Lee & Yianneskis [16].

It has been observed, over the past 10 years, that static mixers are most appropriate for fulfilling good mixing with efficient heat transfer. However, for some specific process and reaction conditions, designing and selecting appropriate equipment is not a trivial task. For fast exothermic reactions in turbulent flows; the main difficulties arise from the complex interactions among flow conditions, chemical process and heat transfer, and predicting the progress of a reaction in a given reactor thus requires detailed study of these three interrelated phenomena.

In this study, we focus on the mixing in a flow of homogeneous viscosity. The more general and close to the application case of reactive mixing is complicated by heterogenous distribution of the viscosity and other thermophysical properties and hence yield different flow structures. The motionless mixer-reactor is constituted of a straight tube of circular inner cross-section along which are fixed vortex generators, trapezoidal tabs that generate longitudinal vortices in the flow direction and thus promote turbulence level and heat transfer. Joshi and Shah [17] made a review of recent progress of heat transfer enhancement through the use of longitudinal vortices in heat exchangers. They describe both active and passive implementations. In the case of passive methods, special surfaces are needed to generate specific vortices. These surfaces are referred to as vortex generators, or turbulence promoters. In a review article, Fiebig [18] explains that vortices increase the rate of kinetic energy flux

and change transition Reynolds number, temperature profiles and their gradients at the wall. They enhance friction and heat transfer.

If vortices embedded in boundary layer flow have been studied intensively because of their importance in aeronautics, in comparison, much less is known about vortices embedded in tube flows, although many different vortex generators have been used. Common vortex generators can be tabs, delta or rectangular wings fixed on a solid surface. The measurement or numerical simulation of momentum and heat transport in these flows is of great importance for many applications (Lau *et al.* [19], Zhu *et al.*[20], Jeong and Ryou [21]).

The aim of this work is the hydrodynamic analysis of the influence of streamwise vortices on the turbulence structure of flow and, in particular the determination of the energy dissipation rate, in a tube equipped with rows of vortex generators. This work is motivated by the special interest in this flow geometry for design and optimization of in-line reactor-heat exchangers used in process industry. The primary mechanism of the induced longitudinal vortex structures is to intensify the mixing process.

Using laser Doppler velocimetry (LDV) equipment to determine the energy dissipation rate directly is difficult, since it requires measuring the spatial derivatives of the velocity fluctuations, which can be done only by measuring the velocity simultaneously in two different positions in space. While some authors have suggested using two separate LDV units (Lee & Yianneskis[16], Michelet *et al.*[15], Wu & Patterson[12]), the energy dissipation rate is most commonly derived from models based on the theory of homogeneous and isotropic turbulence. Corrections are generally used to take into account inhomogeneity and anisotropy.

Two types of models are generally used to derive the energy dissipation rate. The first model, adopted in the present study, estimates the dissipation rate from the turbulence kinetic

energy and a macro length scale. The second model is based on the analysis of turbulence energy spectra.

Estimation of the energy dissipation from turbulence kinetic energy and a macro length scale is based on a dimensional analysis originally suggested by Batchelor [22]. However, the original expression he suggested for the energy dissipation has been verified only for approximately isotropic flows (Hinze [23], Tennekes & Lumley[24]). Additional analyses were initially suggested by Townsend [25], and Tennekes [26] in order to adapt Batchlor's equation for highly anisotropic shear flows. Despite the restricitve assumptions of this model, it has been used successfully to describe the distribution of energy dissipation in stirred tank mixer-reactors (see for example Sato *et al.*[3, 4], Mujumdar *et al.*[5], Rao & Brodkey[6], Komasaawa *et al.*[7], Gunkel & Weber[8], Barthole *et al.*[10], Wu & Patterson[12], Baudou *et al.*[13] as well as Mavros *et al.*[14]).

The turbulence energy dissipation rate has also been estimated by some authors from energy spectra in stirred-tank mixer reactors (Wu & Patterson[12], Ito *et al.*[27], Nishikawa *et al.*[28], Okamoto *et al.*[29], Barthole *et al.*[30]). This method involves calculating the energy dissipation by integration of the energy spectra. In our case, the relatively large size of measuring volume of LDV allows more than one scattering particle through the interference pattern at a time. This induces the so-called ambiguity noise in the high-frequency range of the power spectra where energy dissipation occurs. Consequently, determining energy dissipation by integration in the frequency domain can lead to large errors. It should be noted that in general other sources of error can contribute to the “ambiguity noise” in the LDV technique, e.g. the data rate, the size of the measuring volume compared to the Kolmogorov scale, optical and electronic noise etc.

The paper is organized as follows. The test section and the global experimental setup are described in section 3. In the present work, the flow inside the motionless mixer-reactor was first analyzed by visualizations using the laser-induced fluorescence technique (LIF) in order to investigate the role of the vortical structures in radial transport. These results are presented in section 4. Mean velocity and turbulent quantities, measured by laser Doppler velocimetry (LDV), and the distributions of macro length scales of turbulence, and the turbulent energy dissipation are described and discussed in section 5. Concluding remarks are presented in section 6.

3. Experimental set up and procedures

This section gives a detailed description of the test section, experimental setup and methods used in this study.

3.1 Test section

The test section is a straight circular tube of 20 mm inner diameter along which seven tab arrays are fixed, as shown on Figure 1. Each of the seven arrays consists of four trapezoidal tabs positioned at 90° to each other in the tube cross-section. The tabs are trapezoidal shaped (7mm x 4mm) and fixed at a 30° angle to the wall. Their main role is to generate a cascade of longitudinal vortices superposed on the basic turbulent flow. The test section is made of mirror-polished perspex with optical-quality surfaces that readily allow flow visualization and LDV measurements. The test section is 180 mm long and the distance between two successive tab arrays is 20 mm (one tube diameter).

The test section is preceded by a preconditioner (2000 mm inox and 300 mm transparent circular tubes) and followed by a postconditioner (300 mm straight transparent circular tube).

The pre-conditioner is used to provide a fully developed flow at the inlet of the test section, and the post-conditioner is used to observe the effects of the test section on mixing quality of the flow. Care was taken that the connections between the test section and both pre-conditioner and post-conditioner did not introduce any perturbation in the flow.

3.2 Description of the basic flow

The role of the tabs is to generate longitudinal vortical structures and intensify turbulence, thus decreasing the characteristic length of micromixing. As the fluid flows along one tab, a wake forms downstream. Due to the angle between the tab and the tube wall, the fluid velocity beneath the tab is much lower than that on top. As a consequence, the pressure on top of the tab drops below the pressure beneath, and a pair of counter-rotating vortices is generated. The cross-section of each vortex pair is mushroom-shaped.

As will be seen later, the vortices enhance radial mass transfer and increase the turbulence level in the flow core.

3.3 Global experimental set up

Experimental study of the flow through the test section entailed flow visualizations by laser-induced fluorescence and laser Doppler velocimetry measurements. All experiments were run with water as working fluid. The flow is provided by a feeding tower that allows working in either an open or a closed loop. Water flows from the reservoir either by gravity or via a centrifugal pump, depending on the desired flow rate. The flow rate is controlled by a valve and measured by a bank of three flowmeters with overlapping ranges (this allows selecting the most appropriate flowmeter for flow rates ranging between 0.5 l/min and 100 l/min). Uncertainty in the flow rate measurements is thus less than 1.6 %. Water then

flows through the pre-conditioner, the test section and the post-conditioner. The water temperature is measured by an 80 μm thermocouple probe at the inlet of the test section to determine its physical properties (viscosity, density) for calculation of the Reynolds number.

For flow visualizations, a dye tracer is injected parallel to the flow direction through an injector of 0.25 mm inner diameter located 10 mm upstream of the first tab array. The radial position of the injector can be adjusted within ± 0.01 mm by a micrometer traversing mechanism (Figure 1). The flow cross-section is illuminated by an argon ion laser sheet. The laser light crosses a silica bar to generate a laser sheet that is then thinned by a planocylindrical lens. When illuminated by a laser light at 514 nm wavelength, the fluorescence tracer re-emits at a higher wavelength, which allows visualization of the flow cross-section only ; other light reflections are filtered using an appropriate optical filter.

Longitudinal flow cross-sections are then viewed by a Hitachi 3CCD high-resolution camera equipped with a NIKON AF MICRO NIKKOR lens of constant focal length (50 mm). Both the camera and the laser-sheet generator are fixed to a rigid frame so that no relative movement between them is possible. The frame is mounted on a traversing mechanism. An electronic displacement ruler allows the movement of the laser sheet in 0.02 mm increments. The position of the laser sheet along the test section can be read on a digital liquid crystal display. This combination lets us follow the longitudinal evolution of the cross-section of streamwise vortices very closely. Images from the camera can be recorded on a Sony "Umatic" video recorder or recorded and processed on a microcomputer. Since the optical axis of the CCD camera makes a non-zero angle with the normal to the laser sheet plane, the recorded visualization images are distorted. The original images are retrieved by applying an optical correcting algorithm to the digitized images. More detailed information about the techniques used for flow visualization is given in Peerhossaini and Weisfreid [31].

4. Flow visualizations

Three series of flow visualizations were performed. We first obtained a global view of all the vortical structures in the test section by injecting blobs of dye intermittently into the flow core. Then injecting a dye filament continuously close to the tube wall let us follow the evolution of a single vortex pair. In these two series of experiments, only the flow cross-section was illuminated by a laser sheet. Finally, longitudinal illumination of the flow allowed visualization of transverse hairpin vortices riding on top of the streamwise vortices.

All flow visualizations were performed at Reynolds number (based on tube diameter) 1000. At this nominal Reynolds number the flow in the preconditioner is fully laminar. As will be seen, vortices developing inside the test section accelerate the transition to turbulence.

4.1 Global visualization of the vortices

Global views of the vortices generated in the flow were visualized by injecting blobs of dye intermittently into the flow core. Dye was introduced through a syringe connected to the injector located 10 mm upstream of the first tab array. Due to the parabolic axial velocity the injected dye in the core region was rapidly advected downstream of the flow. On the other hand, since the velocity close to the wall was much lower, a thin film of dye remained in the vicinity of the tube wall, letting us visualize the streamwise vortices developed close to the wall.

A photograph of the flow cross-section 2 mm downstream of the first tab array is shown in Figure 2a. It can be seen that each tab generates a pair of counter-rotating vortices of mushroom-shaped cross-section. The height of the vortices is of the same order as the height

of the tabs. At this position, video visualizations show that the vortices remain stable until the second tab array is reached.

Figure 2b shows a photograph of the flow cross-section visualized 2 mm downstream of the second tab array. At this position, two pairs of vortices can be seen on top of each tab. The vortices generated by the first tab array are still visible ; they have been pushed up towards the tube centerline by new vortices generated by the second tab array. This mechanism results in vortex superposition, and video visualizations show that the observed vortices begin to oscillate slowly.

Vortex superposition was also observed downstream of the subsequent tab arrays. However, the observed vortices oscillate at higher and higher frequencies. Downstream of the fourth tab array, the vortices break up into an apparently turbulent motion. Organized structures were no longer steadily observed. Such turbulent motion downstream of the fourth tab array was observed even at Reynolds numbers below 1000, and is a consequence of the breakdown of the superposed longitudinal vortices.

4.2 Longitudinal evolution of a single pair of vortices

Experiments were carried out to study the effects of longitudinal vortices on radial transport of a passive tracer. For this purpose, a dye filament was injected continuously through an injector positioned 0.5 mm from the wall. Experiments were run at Reynolds number 1000; at this Reynolds number, the flow inside the preconditioner is laminar and the dye streak is a straight line before reaching the first tab.

Figure 3 shows photographs of the dye filament cross-section visualized 2 mm downstream of the first, second, fourth and fifth tab arrays. As the tracer filament reaches the first tab, the dye rolls up around the vortices. Downstream of the second tab, the dye is pushed

towards the tube centerline by a new pair of vortices. The vortices generated by the first tab array are still discernible but have been strongly deformed, and dye begins to spread towards the flow core. This radial transport of the dye increases as the fluid flows downstream of the test section. Downstream of the fourth tab array, the tracer dye is no longer trapped in the vortices generated by a single tab, and organized structures can no longer be observed. Video visualization shows that the structures oscillate at high frequencies in a random way. At this position, the flow appears turbulent but homogeneous mixing is not yet achieved. Downstream of the fifth tab array the tracer dye tends to occupy the whole cross-section and mixing is further enhanced by the subsequent tab arrays.

These visualizations (with a continuous injection of dye filament) have revealed the role of the longitudinal vortices in the radial transport mechanism. It is important to recall that the experiments were performed at Reynolds number 1000. At this Reynolds number, in the straight tube preceding the static mixer, radial mass transport occurs only by molecular diffusion. At higher Reynolds numbers corresponding to turbulent flows, radial mass transport by the generated vortices will be superposed on the transport mechanism inherent in the background turbulent flow.

4.3 Visualization of hairpin vortices

The two preceding sections described the visualization of longitudinal structures using cross-sectional flow. Longitudinal illumination of the test section reveals that hairpin vortices also develop that ride on top of the main longitudinal vortices, as shown in Figure 4. Their contribution to the radial transport mechanism is less than that of the longitudinal vortices.

As can be seen in Figure 4, hairpin vortices are generated periodically. As a consequence, they are separated by a constant wavelength (α). Downstream of the fourth tab

array, the hairpin vortices break up; this is in agreement with the random motions observed on the flow cross-section visualizations (see Figure 3, fourth tab array).

5. Velocity field measurements

Here we present the results of velocity measurements obtained by laser Doppler velocimetry (LDV). Time-averaged velocity values (called mean velocity) as well as turbulence intensity fields were measured. However, integral scales and turbulent energy dissipation rates were of particular interest in this work because of their usefulness in modeling local micromixing rates in turbulent flows.

5.1 Apparatus and data acquisition

The measurements presented in this section were performed by using a two-component DANTEC LDV system with two BSA-enhanced signal-processing units (57N20 BSA and 57N35 BSA-enhanced models). A lightweight precision three-dimensional traversing mechanism was used to displace the measuring volume. To enhance the data acquisition rate, all measurements were performed in forward-scattering mode. In addition, the working fluid was seeded with small particles of Merck Iriodine 111. The focal length of the emission lens was 160 mm and that of reception was 80 mm. The dimensions of the measuring volume was $dx = 697 \mu\text{m}$, $dy = 84 \mu\text{m}$ and $dz = 84 \mu\text{m}$, where dx denotes the size of the measuring volume in the radial direction. The data acquisition rate was 1.5 to 2 kHz and the sampling time was 5 seconds.

In the present study, because of the external form of the test section, refraction phenomena could not be avoided without changing either the test section material or the working fluid. For this reason, measurements were limited to the mean and fluctuating

components of the axial velocity on a horizontal plane passing through the center of the test section. In fact, the effects of refraction phenomena are minimized in the symmetry plane. Measurements were made for different Reynolds numbers in order to follow the evolution of the axial velocity profile along the test section; the results are presented below.

5.2 Mean velocity field

Here we describe the longitudinal evolution of the mean axial velocity profiles measured 2 mm downstream of each tab array at Reynolds number 10000. The effects of Reynolds number will be studied by comparing similar results obtained at $Re=1500$, 3000 and 15000. In all curves, axial velocity is scaled by the bulk velocity.

5.2.1 Longitudinal evolution of the velocity profiles

Figure 5 shows profiles of the mean axial velocity measured in the straight tube preceding the first tab array (post-conditioner) for Reynolds number equal to 10000. Two profiles were measured at 30 mm and 70 mm upstream of the first tab array. The third profile corresponds to the experimental Nikuradze[32] velocity profile in a fully developed turbulent flow through a straight circular tube. As can be seen in the figure, the three curves are almost collapsed, confirming that the flow is fully developed before reaching the first tab array.

Figure 6 shows three profiles of the mean axial velocity, two measured 2 mm upstream and 2 mm downstream of the first tab array and the third obtained 2 mm downstream of the second tab array. Axial locations of the profiles are indicated by vertical lines on the schematic diagram of the test section shown as an insert on the figure. The velocity profile 2 mm upstream of the first tab array is similar to that in the preconditioner. The acceleration of the axial velocity observed downstream of the first tab array is due to the blockage of the flow cross-section caused by the tabs. The second tab array has a more pronounced effect on

the axial velocity profile : two minimum values give rise to a significant deformation of the velocity profile, which becomes W-shaped. The observed minimum values, close to the tube wall, show the existence of a radial momentum transport mechanism. In fact, streamwise vortices transport low-momentum fluid particles from regions close to the wall towards the tube center. This reduces the velocity magnitude and minimum values are observed. On the other hand, high-momentum fluid particles, initially situated in the flow core, move towards the tube wall and thus accelerate in this region.

A global view of the evolution of the mean axial velocity profiles is shown in Figure 7. The first profile corresponds to the measurements upstream of the first tab array and the subsequent ones were measured 2 mm downstream of each tab array designated with the tab number. The observed "W" deformation becomes more pronounced after the third tab array, indicating an intensification in the radial momentum transport. After the fourth tab array, no further evolution is observed in the mean axial velocity profile.

5.2.2 Effect of Reynolds number

Global views of axial velocity profiles obtained for Reynolds numbers 1500 and 3000 are shown in Figures 8 and 9. Note that each set of profiles corresponds to a different hydrodynamic regime in the straight tube preceding the first tab array: Reynolds number 1500 corresponds to fully laminar flow, Reynolds number 10000 to fully turbulent flow and Reynolds number 3000 to a transitional regime.

When the flow in the pre-conditioner is fully laminar ($Re=1500$), the axial velocity profile is parabolic before reaching the first tab array. The "W" deformation appears only downstream of the third tab array. At this location the deformation is very pronounced, but it begins to vanish after the subsequent tab arrays. This evolution in the axial velocity profiles

suggests a interaction between two mechanisms of momentum transport. The first mechanism, induced by the streamwise vortices, tends to generate the "W" deformation by moving low-momentum fluid particles from the wall region to the core flow and vice versa. The second mechanism, inherent in the velocity fluctuations due to the unsteadiness, tends to homogenize the momentum distribution in the flow cross-section and thus to reduce the "W" deformation. This is in agreement with the flow visualization experiments, where unsteady motion appears only after the fourth tab array is reached. Therefore, the mechanism associated with turbulent velocity fluctuations becomes more significant beyond this location.

At Reynolds number 3000, the flow field can be considered as in a transitional flow state. The mean axial velocity profile measured upstream of the 1st tab array is not regular ; spatial oscillations can be observed. At this regime the flow is mainly laminar, but turbulent slugs appear intermittently (Hinze [23]). Increasing the Reynolds number tends to increase the length of the turbulent slugs as well as the frequency at which they appear. The spatial oscillation observed can be explained by the presence of these turbulent slugs. Spatial oscillations persist downstream of the first tab array however, the "W" deformation begins to appear downstream of the second tab array, is amplified by the third tab array, and then decreases. This decreasing deformation suggests that the flow becomes fully turbulent after the fourth tab array and thus tends to homogenize the momentum distribution.

We also conducted experiments for Reynolds number 15000 (not shown here), the flow in the pre-conditioner preceding the first tab array is already fully turbulent. Measured axial velocity profiles show the same features as observed at Reynolds number 10000. A "W" deformation appears downstream of the second tab array, with an amplitude smaller than that observed at $Re=1500$. In fact, turbulent velocity fluctuations tend to homogenize the momentum distribution.

To summarize, the evolution of the mean axial velocity profile in the test section depends on the flow regime upstream of the first tab array. It is suggested that two mechanisms of momentum transport are competing in the flow. The first mechanism, due to the vortical structures, tends to generate the "W" deformation. The second mechanism, associated with turbulent velocity fluctuations, tends to homogenize the momentum distribution. For low Reynolds numbers, corresponding to a laminar regime in the preconditioner, the latter mechanism does not appear until the fourth tab array is reached.

5.3 *Turbulence intensity field*

The turbulence intensity of the axial velocity is calculated using the expression

$$T_u = \frac{\sqrt{u^2}}{U} \cdot 100 \quad (1)$$

where u is the fluctuating part of the instantaneous velocity and \bar{U} is the mean axial velocity.

Figure 10 shows the evolution of the turbulence intensity profiles in the test section for Reynolds number 10000. The first profile was measured in the preconditioner preceding the first tab array, while the following ones correspond to measurements obtained 2 mm downstream of each tab array.

In the straight tube preceding the first tab array, the turbulence intensity profile is "U"-shaped, with minimum value 6% at the tube center and two maxima of about 25% close to the tube wall. This profile is typical of a fully developed turbulent flow inside a straight tube (see for example Hinze [23]), and confirms that the flow is fully developed before entering the test section.

After flowing through the first tab array, the turbulence intensity decreases and the profiles become flatter. The decrease in turbulence intensity is due to the acceleration of the mean axial velocity observed across the first tab array (see Figure 6). The second tab array induces a more significant deformation on the profile. The turbulence intensity is increased substantially but not uniformly: two maxima appear at a distance from the tube wall equivalent to the tabs' height. Turbulence intensity is further increased by the third tab array, but then an established periodic regime is reached downstream of the fourth array. The global representation in Figure 10 shows that the turbulence intensity is substantially increased in the core flow by the tabs. However, the turbulence distribution is not uniform even at the test section exit.

Figure 11 shows the longitudinal evolution of the turbulence intensity measured 4 mm from the tube wall; the small triangles designate the tab array locations. The turbulence intensity decreases from 6% to 5% across the first tab array because of flow acceleration in the axial direction. Downstream of the first tab array, the longitudinal vortical structures generate more turbulence, leading to a linear increase of turbulence intensity up to 17.5% upstream of the third tab array. Beyond this location, the curve begins to oscillate and reaches an established periodic regime downstream of the fourth tab array. Detailed observation of this periodic regime reveals that turbulence intensity tends to decrease across the tab arrays and increase between them. Periodic acceleration and deceleration of the mean flow is the underlying mechanism in this behavior. In fact, when the fluid flows across a tab array, the apparent flow cross-section is reduced, leading to an acceleration of the mean flow. Similarly, between the tab arrays the flow cross-section is enlarged, inducing flow deceleration at these locations.

The turbulence intensity field was measured for Reynolds numbers ranging from 7500 to 15000. In this range, no influence of the Reynolds number was observed on the distribution of turbulence intensity. For lower Reynolds numbers, measured velocity fluctuations were of the same order of magnitude as the resolution of the velocimeter, so that these results were not taken into account. The following section describes the evaluation and distribution of turbulence macro scales.

5.4 Turbulence macro scale

The Eulerian turbulence macro scale is an important attribute of turbulent flows in chemical-reactor-heat exchangers, since it is the scale of the eddies that contain turbulence energy. In homogeneous turbulent flows, the integral macro scale is defined as :

$$\Lambda = \int_0^\infty \frac{\overline{u(x_0)u(x_0+\xi)}}{u'^2} d\xi \quad (2)$$

where x_0 is a spatial coordinate and u the fluctuating velocity component.

The integral scale can be evaluated by integrating the measured space velocity correlations, which requires using two points measurements. Moreover, measurements must be performed continuously and simultaneously in time. Since LDV works discontinuously, it is not very well suited for such measurements. In addition, the apparatus used for the present study cannot take measurements at two spatially separated points.

As a consequence, integral scales were converted from time correlations, with suitable convection velocities U_{conv} , as follows :

$$\Lambda = U_{conv} \sigma \quad (3)$$

where σ is the time macro scale.

Evaluation of the integral macro length scales with this method obviates the difficulties inherent in direct measurement of spatial correlations. Our determination of σ and U_{conv} is described in the two following sections.

5.4.1 Evaluation of integral time scales

The integral time scale of the velocity fluctuations u is defined by the following expression (Hinze [23]) :

$$\sigma = \int_0^\infty \frac{\overline{u(t_0)u(t_0+\tau)}}{u^2} d\tau \quad (4)$$

This is a time scale after which fluctuations of a velocity U are no longer correlated. The integral time scale can be evaluated from the temporal correlation function, which requires measurements of the velocity with only one single probe. Measurements must be performed at sufficiently short time intervals to detect high-frequency fluctuations. Laser Doppler velocimetry allows such fast measurements by optimizing seeding and optical adjustments. However, since LDV measurements are not performed at constant time intervals, the data must be re-sampled. In the present study, all data were re-sampled according to a method suggested by Høst-Madsen and Caspersen, as described in more details in Høst-Madsen [33] and Høst-Madsen & Caspersen [34].

5.4.2 Evaluation of a convection velocity U_{conv}

The convection velocity in equation 3 can be approximated by the mean local velocity if Taylor's hypothesis is permitted ; that is, if temporal fluctuations are assumed equivalent to

instantaneous spatial fluctuations that are convected by the mean velocity field. This hypothesis is valid for very limited flows where the turbulence is approximately homogeneous, such as grid-generated turbulence. Nevertheless, Taylor's hypothesis has already been used by various authors to transform temporal results into spatial results in more complex flows such as flows in batch chemical reactors (Sato *et al.* [3, 4], Mujumdar *et al.*[5], Rao & Brodkey[6], Komasaawa *et al.*[7], Barthole *et al.*[10], Baudou *et al.*[13], Mavros *et al.*[14]). Baudou *et al.*[13] indirectly verified their results by comparing the obtained distribution of turbulence energy dissipation rate. The authors showed that satisfactory results can be obtained except in regions where the flow is strongly three-dimensional. This point is discussed in more detail in the next section. However, for high-intensity turbulent shear flows, such as the flows in chemical reactors, the applicability of Taylor's hypothesis is questionable. In this study, the convective velocity U_{conv} was estimated by a method suggested by Heskestad [35], who derived an expression for the convective velocity from the equations of motion in rectangular coordinates. If only one component of the velocity exists, the expression derived by Heskestad [35] reads :

$$U_{conv}^2 = \bar{U}^2 \left(1 + \frac{\bar{u}^2}{\bar{U}^2} + 2 \frac{\bar{v}^2}{\bar{U}^2} + 2 \frac{\bar{w}^2}{\bar{U}^2} \right) \quad (5)$$

assuming $V=W=0$. Van Doorn[1981] extended this expression to three-dimensional flows

$$U_{conv}^2 = \bar{U}^2 \left(1 + 2 \frac{\bar{V}^2}{\bar{U}^2} + 2 \frac{\bar{W}^2}{\bar{U}^2} + \frac{\bar{u}^2}{\bar{U}^2} + 2 \frac{\bar{v}^2}{\bar{U}^2} + 2 \frac{\bar{w}^2}{\bar{U}^2} \right) \quad (6)$$

Goldschmidt *et al.*[36] found a similar result from measurements performed in a plane jet. In the present study, equation 6 was used as simplified by the following hypotheses :

- the axial velocity component is much larger than tangential and radial components ($\overline{U} \gg \overline{V}$ and $\overline{U} \gg \overline{W}$);
- velocity fluctuations are locally isotropic ($v' \approx u'$ and $w' \approx u'$)

The first hypothesis is easily justified from geometrical considerations : in the axial symmetry plane examined here, no tangential velocity component can exist ($\overline{V} = 0$). In addition, radial velocities are much smaller than the axial velocity (typically a few millimeters).

Concerning the second hypothesis, the experimental results verify that the rms values of tangential and axial velocity fluctuations are effectively of the same order ($v' \approx u'$). However, since the radial component of the velocity could not be measured (for optical reasons), we simply asserted by symmetry analysis that fluctuations of this component are of the same order of magnitude as the fluctuations of the axial component ($w' \approx u'$).

The above hypotheses let us simplify equation 6 as follows

$$U_{conv}^2 = \overline{U}^2 \left(1 + 5 \frac{\overline{u'^2}}{\overline{U}^2} \right) \quad (7)$$

This expression is in good agreement with Lumley [37], who studied temporal spectra measured in a strongly turbulent sheared flow. This analysis showed that $(1 + 5 \overline{u'^2} / \overline{U}^2)$ is effectively the factor needed to correct the velocity scale obtained from Taylor's hypothesis.

5.4.3 Distribution of macro length scale

Figure 12 shows four profiles of the macro length scale calculated with equation 3 at Reynolds number 10000. The first profile was measured upstream of the first tab array, and

the others correspond to positions 2 mm downstream of the first, third and fifth tab arrays, respectively. The solid lines are polynomial fittings of experimental data.

In the straight tube preceding the first tab array, the profile of the macro length scale is "U"-shaped, with a minimum value of 4 mm at the tube center and two maxima close to the tube wall. Downstream of the first tab array, two maxima appear 4 mm from the tube wall, a distance equivalent to the tabs' height. The subsequent tab arrays do not introduce any more qualitative modification to the distribution of turbulence macro length scale, except that the macro length scale increases progressively up to the fifth tab array.

As can be seen from the curves, the macro length scale reaches a maximum value of around 10 mm. Since turbulence energy is mainly supplied by the longitudinal vortex structures in the test section, this 10 mm maximum indicates that these structures should be larger than revealed by visualizations.

5.5 Distribution of local turbulence energy dissipation

Local turbulence energy dissipation is an important parameter in chemical reactors since it governs the size of the smallest turbulent eddies in the flow. In fact, according to Kolmogorov's energy-cascade theory, the energy of turbulence is transferred from large-scale eddies to smaller ones. The process proceeds with no transformation of kinetic energy into heat as long as the size of the eddy is greater than the Kolmogorov's micro scale λ .

This energy-cascade model suggests that large-scale eddies are governed by external geometry parameters and forces, and that they contain all the energy that can be dissipated, the energy dissipation ε is necessarily governed by them. Smaller-scale eddies are governed by the fluid viscosity and turbulence energy dissipation rate ε . The range of Kolmogorov scales, $(\varepsilon/\nu)^{1/2}$, becomes a fundamental parameter for all phenomena occurring at these scales. The

selectivity of fast exothermic reactions in turbulent flows is directly related to the distribution of ε (Baldyga & Bourne [1], Laufhütte & Mersmann [11]). In fact, this parameter plays a leading part in the interaction between the flow dynamics and the evolution of the chemical reaction. For this reason much work on turbulent flows in chemical reactors has focused on determining ε .

Lawn [38] measured the energy dissipation in an air flow through a straight tube of circular cross-section at large Reynolds numbers. He used an indirect method entailing measuring production and diffusion terms of turbulence; the dissipation rate is then deduced from a balance equation. Instead of measuring the pressure-velocity correlations \overline{vp} , Lawn [38] evaluated them from triple velocity correlations, using a simplifying analysis based on orders of magnitude.

In the present study, turbulence energy dissipation was measured directly. The general definition of turbulence energy dissipation is given by the following expression and approximated by assuming that small structures which contribute to the dissipation mechanism are characterized by locally isotropic high frequency fluctuations:

$$\varepsilon = \nu \sum_{i,j} \overline{\left(\frac{\partial u_i}{\partial x_j} + \frac{\partial u_j}{\partial x_i} \right) \frac{\partial u_i}{\partial x_j}} \approx \nu \sum_{i,j} \overline{\left(\frac{\partial u_i}{\partial x_j} \right)^2} \quad (8)$$

where u_i represents the velocity fluctuation in the x_i direction.

However, measurement of spatial derivatives requires the use of a two-probe velocimeter, which could not be achieved with the LDV equipment used in the present study. In addition, the relatively large measurement volumes with LDV let more than one scattering particle through the interference pattern simultaneously. This induces a so-called ambiguity noise in the high-frequency range of the power spectra, where energy dissipation occurs, so

that determining the energy dissipation by integration in the frequency domain can lead to large errors.

An attempt was then made to find a simpler way to evaluate the energy dissipation, and a method based on Batchelor's model of energy cascade (Batchelor [22]) was adopted. Using a dimensional analysis, Batchelor [22] suggested that the energy dissipation should be written as :

$$\varepsilon = \frac{3}{2} C \frac{\overline{u^2}^{3/2}}{l_e} \quad (9)$$

Batchelor [22] showed that the value of C is of the order of 1 in the case of an approximately isotropic grid-generated turbulence. Some results obtained with equation 9 have been confirmed experimentally in different approximately isotropic flows (see for example Hinze [23] or Tennekes & Lumley [24]). Nevertheless, the validity of this equation for highly anisotropic shear flows is not so evident. Townsend [25] and Tennekes [26] have suggested the following expression

$$\varepsilon = C \frac{q^{2/3}}{l_e} \quad (10)$$

where q represents turbulence kinetic energy.

Assuming that high-frequency fluctuations (which are involved in the dissipation process) are locally isotropic allows determination of ε by measuring only one velocity component. Furthermore, the maximum value of the inertial range l_e can be approximated, as usual, by the integral macro length scale Λ . The local turbulence energy dissipation rate can then be approximated by the expression :

$$\varepsilon \approx C \frac{\left(\frac{3}{2}\overline{u^2}\right)^{3/2}}{\Lambda} \quad (11)$$

The value of the empirical constant C has been the subject of many studies. In a nearly isotropic grid-generated turbulence flow, Batchelor [22] found a value of about 1.0, a value also obtained by Antonia *et al.*[39] in a circular jet. However, the latter authors obtained a value of 0.5 from measurements performed in a plane jet. Wu & Paterson [12] measured the velocity field in a turbulent mixed tank and estimated the energy dissipation from an energy balance, in so doing verifying the validity of equation 11. They also deduced a value of $0.85 \pm 10\%$ for the constant C .

Similar measurements in a turbulent stirred tank were made by Baudou *et al.*[13]. They estimated the energy dissipation rate from power spectra and also by using an expression similar to equation 11, by comparing of the results, they found a value of C of 2.4. It can thus be concluded that C has no universal value, but depends on the flow characteristics.

In the present study, the constant C was evaluated in two steps. The first step involved calculating the ratio ε/C from the experimental results ($\overline{u^2}$ and Λ) obtained in the straight tube preceding the first tab array. This is equivalent to calculating ε from equation 11 but with the value of C fixed at 1. The second step was to compare this ratio with the experimental energy-dissipation results obtained by Lawn[38] in a straight circular tube, with conditions similar to this experiment. Knowing the values of ε/C and ε permits deduction of C . The results of this comparison are presented in Figure 13, which plots two qualitatively similar "U"-shaped curves, giving a value of C for each position. However, in the present study, C was fixed at 1.8, which represents the mean value for all positions.

Figure 14 shows eight profiles of turbulence energy dissipation for Reynolds number 10000. The first profile corresponds to measurements obtained upstream of the first tab array and the others are located downstream of each tab array. Solid lines indicate polynomial fitting of the experimental data. In the straight tube preceding the first tab array, the energy dissipation has a "U"-shaped profile with a minimum at $0.0075 \text{ m}^2 \text{ s}^{-3}$ at the center and two maxima close to the walls. No perceptible modification is observed immediately downstream of the first tab array. The second tab array induces an important deformation on the profile, similar to that observed in turbulence intensity profiles: two maximum values of $0.3 \text{ m}^2 \text{ s}^{-3}$ appear close to the wall at a distance equivalent to the tab height, which is the position where the vortices are generated. A minimum value of $0.02 \text{ m}^2 \text{ s}^{-3}$ is also observed at the center. The third and fourth tab arrays have no effect on the maximum values of ε , but the minimum value increases considerably at the tube center. An established periodic regime seems to be reached after the fifth tab array.

It can be observed that the distribution of turbulence energy dissipation is not uniform even at the exit of the seventh tab array. This heterogeneous turbulence distribution is in good agreement with the numerical results of Lauschke[40] and Phillips *et al.*[41], who performed a numerical simulation of an exothermic reaction in a continuous reactor similar to the test section here, for a Reynolds number of 15000. The amount of heat produced was dependent upon the micro scales and the reactant was injected at the tube center. The results showed an overheated zone of annular cross-section, corresponding to the region in the present study where ε is maximum, indicating a higher reaction rate at this region.

The energy dissipation was also evaluated from the experimental results obtained here at Reynolds number 15000 in order to analyze the effect of this parameter. The results showed no qualitative modification of the distribution of ε . Increasing the Reynolds number does not

homogenize the distribution, but the values of ε tend to increase globally, indicating a decrease in the characteristic scales of dissipative eddies.

6. Concluding remarks

An experimental hydrodynamic study was carried out to provide detailed information on the flow through an in-line reactor-heat exchanger. The influence of streamwise vortices on the integral scales and turbulent energy dissipation rates were the particular objectives of this work because of their usefulness in modeling local micromixing rates in turbulent flows. The geometry of the test section was a straight tube in which trapezoidal tabs are inserted.

The first step of the work was to make flow visualizations by a laser-induced fluoresceine technique. Global visualizations obtained by intermittently injecting blobs of tracer revealed the hydrodynamic structures produced by the tabs. Their role in radial mass transfer was also observed by following the evolution of a dye tracer filament injected continuously. Finally, longitudinal illumination of the test section let us visualize small transverse hairpin vortices, whose contribution to the radial mass-transport mechanism is less than that of the longitudinal vortices.

Results on the mean velocity distribution showed that the longitudinal vortices have an important role in radial mass transport. They generate a "W" deformation of the mean velocity profile by moving low-momentum fluid particles from the wall vicinity towards the flow core, and vice versa. Analysis of the effects of Reynolds number on the mean velocity distribution revealed that two mechanisms of transverse momentum transport are in competition. The momentum transport associated with longitudinal vortices tends to increase the deformation, while turbulent diffusion tends to homogenize the momentum distribution.

Our results also showed that the vortices substantially increase the turbulence intensity in the flow, from 5% to 17%. This increase in turbulence is achieved progressively: a development length equivalent to three tab arrays is necessary to reach a stable periodic regime.

The next step of the analysis focused on the integral scale distribution. To avoid difficulties inherent in the measurement of time-space correlations, integral scales were determined using Taylor's hypothesis, with appropriate corrections for convective velocities. The distribution of the integral scales suggested that the vortical structures should be larger than those visualized.

The information on integral scales allowed estimation of the energy dissipation distribution, an important parameter in predicting the selectivity of fast chemical reactions. Our estimate of the energy dissipation was based on Batchelor's dimensional analysis; results showed that the energy dissipation is increased substantially but not uniformly in the cross section by vortex generators. An annular region of high dissipation was observed, a result that explains previous results involving exothermic fast chemical reactions. In addition, the information on energy dissipation will help in optimizing reactant injection.

The complex geometry of the mixer did not allow measurement of the velocity and turbulent quantities in three dimensions. Some strong assumptions thus had to be made in order to extract the turbulence properties from the one-dimensional LDA measurements. Of these assumptions, the strongest were the axial symmetry of the flow and the homogeneous nature of the turbulence. Also, for the Taylor hypothesis to be valid, the mean flow velocity must be constant and the turbulence intensity should not exceed 20%. These two conditions are satisfied in the present work, although the turbulence intensity is at its maximum permissible value. In order to verify (*a posteriori*) the appropriateness of these assumptions,

some (one-dimensional) measured turbulence properties are examined here and their trends are compared with typical trends in turbulent flows.

Figure 15 and 16 show the temporal autocorrelation coefficients of the axial velocity

$$\left(\rho(x_0, \tau) = \frac{\overline{u'(x_0, t)u'(x_0, t + \tau)}}{\overline{u'(x_0, t)u'(x_0, t)}} \right) \text{ for two positions : one upstream of the first tab array (Figure$$

15) and the other downstream of the 7th tab array (Figure 16). The flow Reynolds number is 15000 and the other autocorrelation coefficients $\rho(\tau)$ are measured at different radial distances (Y/R ; $Y=0$ corresponds to the wall position) from the mixer wall. As shown in Figure 15, the general trend of the curves is similar to typical autocorrelation coefficient curves reported in the literature, with an exponential decrease of the autocorrelation coefficient with time. The curves are grouped together, with, however, a greater decrease in $\rho(\tau)$ for positions farther from the wall. The integral time scale T , defined as $T = \int_0^{\infty} \rho(\tau) d\tau$, varies between 45 ms (close to the wall) and 20 ms (at the mixer center).

Figure 16 shows the evolution of the temporal autocorrelation coefficient for the axial position 2 mm downstream of the 7th tab array. One observes the same exponential decrease of $\rho(\tau)$ with time, and here the temporal integral time scale varies between 10 ms and 2 ms.

The appropriateness of the assumptions is also verified by comparing the maximum value of the local turbulent dissipation rate ε_{\max} obtained from the one-dimensional LDA measurements with the volume-averaged dissipation $\bar{\varepsilon}$ obtained from the pressure drop between the entrance to and exit from the mixer :

$$\bar{\varepsilon} = \frac{U \cdot \Delta P}{\rho L} \text{ (W.Kg}^{-1}\text{)} \quad (12)$$

where L is the mixer length and U is the mean velocity in the mixer. This can give an order-of-magnitude comparison of the ε values measured in two different ways. Figure 17 shows the ratio $\frac{\varepsilon_{\max}}{\bar{\varepsilon}}$ as a function of the axial position x in the mixer for Reynolds number 15000. The two first (leftmost) points on the curve ($x \approx 15$ mm and 20 mm) respectively correspond to downstream of the first tab array and upstream of the second tab array, where the turbulent dissipation rate is not yet enhanced by the vortex generators. The experimental points at $x \approx 30$ mm and 50 mm respectively represent the downstream end of the second tab array and the upstream end of the third one, where the turbulent dissipation rate is enhanced and reaches its local maximum value on top of the third tab array. Ultimately, the last (right most) point corresponds to downstream of the 7th tab array. From Figure 17 it is evident that beyond the 3rd tab array the maximum local turbulent energy dissipation rate is stabilized (does not evolve any more in the axial direction), and the order of magnitude of ε_{\max} is 4 times $\bar{\varepsilon}$, a reasonable value given the strong difference between the local maximum (near the tab tip) and the local minimum (near the wall and at the center of the mixer) values of ε .

7. References

- [1] J.Baldyga, J.R. Bourne, A fluid mechanical approach to turbulent mixing and chemical reaction, *Chem. Eng. Commun.*, 28(1984), 231-281.
- [2] L.Cutter, Flow and turbulence in a stirred tank. *AIChE J.*, 12(1966), 35-45.
- [3] Y. Sato, K.Ishii, Y. Horie, M. Kamiwano, K.Yamamoto, Turbulent flow in a stirred vessel. *Kagaku Kogaku*, 31(1967), 275- 281.
- [4] Y.Sato, M.Kamiwano, K. Yamamoto, Turbulent flow in a stirred vessel - effects of impeller types. *Kagaku Kogaku*, 34(1970), 104- 111.

- [5] A.S.Mujumdar, B.Huang, D.Wolf, M.E.Weber, W.J.M.Douglas, Turbulence parameters in a stirred tank, *Can. J. Chem. Engng*, 48(1970), 475-483.
- [6] M.A.Rao, R.S.Brodkey, Continuous flow stirred tank turbulence parameters in the impeller stream, *Chem. Eng. Sci.*, 27(1972), 137-156.
- [7] I.Komasawa, R.Kuboi, T. Otake, Fluid and particle motion in turbulent dispersion, *Chem. Eng. Sci.*, 29(1974), 641-650.
- [8] A.A.Gunkel, M.E.Weber, Flow phenomena in stirred tanks, Part I & II., *AIChE J.*, 21(1975), 931-949.
- [9] Y. Okamoto, M. Nishikawa, K. Hashimoto, Energy dissipation rate distribution in mixing vessels and its effects on liquid-liquid dispersion and solid-liquid mass transfer, *Int. Chem. Eng.*, 21(1981), 88-94.
- [10] J.P.Barthole, J.Maisonneuve, J.N.Gence, R. David, J. Mathieu, J. Villermaux, Measurement of mass transfer rates, velocity and concentration fluctuations in an industrial stirred tank, *Chem. Eng. Fundam.*, 1(1983), 17-26.
- [11] H.D.Laufhütte, A. Mersmann, Local energy dissipation in agitated turbulent fluids and its signification for the design of stirring equipment, *Chem. Eng. Thechnol.* , 10(1987), 56-63.
- [12] H.Wu, G.K. Patterson, Laser-Doppler measurements of turbulent flow parameters in a stirred mixer, *Chemical Engineering Science*, Vol.44, No. 10, (1989), 2204-2221.

- [13] C.Baudou, C.Xuereb, J.Costes, G. Ranchin, J.Bertrand, Laser Doppler measurements of flow field and turbulent flow parameters in a stirred tank equipped with two industrial propellers, *Récents Progrès en Génie des Procédés, Edition Technique et Documentation, Lavoisier*, vol 11, 51(1997), 11-18.
- [14] P.Mavros, C.Xuereb, J.Bertrand, Effects of radial or axial impeller and liquid viscosity on energy dissipation in agitated vessels, *Récents Progrès en Génie des Procédés, Edition Technique et Documentation, Lavoisier*, vol 11, 51(1997), 51-58.
- [15] S.Michelet, A.Kemoun, J.Mallet, M.Mahouast, Space-time velocity correlations in the impeller stream of a Rushton turbine, *Experiments in Fluids*, 23, 5(1997), 418-426.
- [16] K.C. Lee, M.Yianneskis, Turbulence properties of the impeller stream of a Rushton turbine, *AIChE Journal*, Vol. 44, Nr. 1,(1998), 13-24.
- [17] A. M. Joshi, R. K. Shah, Heat transfer surface enhancement through the use of longitudinal vortices : A review of recent progress, *Experimental Thermal and Fluid Science*, 11(1995), 295-309.
- [18] M. Fiebig, Embedded vortices in internal flow: heat transfer and pressure loss enhancement , *Int. J. Heat and Fluid Flow*, 16(1995), 376-388.
- [19] S. Lau, K. Meiritz, V. Vasanta Ram , Measurement of momentum and heat transport in the turbulent channel flow with embedded longitudinal vortices, *Int. Journal of Heat and Mass Transfer*, 20(1999), 128-141.
- [20] J. X. Zhu, M. Fiebig, N. K. Mitra, Numerical investigation of turbulent flows and heat transfer in a rib-roughened channel with longitudinal vortex generators, *Int. J. Heat Mass Transfer*, Vol.38, 3(1995), 495-501.

- [21] J. Y. Jeong, H. S. Ryou, Numerical simulation of heat transfer and flow structure in 3-D turbulent boundary layer with embedded longitudinal vortex, *Num. Heat Transfer A*, 31(1997), 433-450.
- [22] G.K. Batchelor, *The theory of homogeneous turbulence*. Cambridge University Press, 1953.
- [23] J.O. Hinze, *Turbulence*, McGraw-Hill, New York, 2nd edn., 1975.
- [24] H. Tennekes, J.L. Lumley, *A First Course In Turbulence*, MIT Press, Cambridge, MA. 1972.
- [25] A.A. Townsend, *The Structure of Turbulent Shear Flow*. 2nd Edition, Cambridge University Press, Cambridge, 1976.
- [26] H. Tennekes, *Turbulence : diffusion, statistics, special dynamics*. In *Handbook of Turbulence*. (Edited by W. Frost and T.M. Moulden), Vol.1, Chap.5, Plenum Press, New York, 1977.
- [27] S. Ito, K. Ogawa, N. Yoshida, Turbulence in impeller stream in a stirred vessel, *Journal of Chem. Engin. of Japan*, Vol. 8, (1975) Nr. 3, 206-209
- [28] Y. Nishikawa, Y. Okamoto, K. Hashimoto, S. Nagata, Turbulence energy spectra in baffled mixing vessels, *Journal of Chem. Engin. of Japan*, Vol. 9, (1976) Nr. 6, 489-494..
- [29] Y. Okamoto, M. Nishikawa, K. Matsuda, K. Hashimoto, Measurement of turbulent diffusion coefficients in mixing vessels, *Int. Chem. Eng.*, 19 (1979), 639-645.
- [30] J.P.Barthole, J. Maisonneuve, J. N. Gence, R. David, J. Mathieu, J. Villermaux, Measurement of mass transfer rates, velocity and concentration fluctuations in an industrial stirred tank, *Chem. Eng. Fundam.*, 1, (1983), 17-26.

- [31] H. Peerhossaini, J.E. Wesfreid, On the inner structure of the streamwise Görtler rolls, *Int. J. Heat and Fluid Flow*, vol. 9, (1988) No.1, 12-18.
- [32] J. Nikuradse, *Gesetzmäßigkeiten der turbulenten Strömung in glatten Rohren*, Verein Deutscher Ingenieure-Forschungsheft, No 356 (1932).
- [33] A. Høst-Madsen, A new method for estimation of turbulence spectra for laser Doppler anemometry, *Seventh International Symposium on Application of Laser Techniques to Fluid Mechanics*, Lisbon. ISBN 3540602364 (1994)
- [34] A. Høst-Madsen, C. Caspersen, The limitations in high frequency turbulence spectrum estimation using the laser Doppler anemometer, *Seventh International Symposium on Application of Laser Techniques to Fluid Mechanics*, Lisbon. ISBN 3540602364 (1994)
- [35] G. Heskestad, A generalized Taylor hypothesis with application for high Reynolds number turbulent shear flows, *Trans. ASME, J. appl. Mech.* 32(1965), 735.
- [36] V.W. Goldschmidt, M.F. Young, E.S. Ott, Turbulent convective velocities (broad band and wave number dependent) in a plane jet, *J. Fluid Mech.*, 105(1981), 327-345.
- [37] J.L. Lumley, Interpretation of time spectra measured in high intensity shear flows, *Phys. of Fluids*, 8(1965), 1056-1062.
- [38] C.J. Lawn, The determination of the rate of dissipation in turbulent flow, *J Fluid Mech.* vol 48(1971), part 3, 477-505.
- [39] R.A. Antonia, B.R. Satyaprakash, A.K.M.F Hussain., Measurements of dissipation rate and some other characteristics of turbulent plane and circular jets, *Phys. Fluids*, 23(1980), 695-700.

- [40] G. Lauschke, A numerical study of exothermic reactions in a wall cooled reactor, *Proceedings of the 1st int. Conf. on Process intensification for the chemical industry*, Antwerp, Belgium, 6-8 December(1995).
- [41] Ch. Phillips, G. Lauschke, H. Peerhossaini, Intensification of batch chemical processes by using integrated chemical reactor-heat exchangers, *Applied Thermal Engineering*, 17(1997), 809-824.

8. Figure captions

Figure 1: Test section, preconditioner and postconditioner

Figure 2: Global flow visualization at two longitudinal positions. $Re=1000$.

a) 2 mm downstream first tab arrays b) 2 mm downstream second tab arrays.

Figure 3: Photographs of the dye filament cross-section inside the static mixer

Figure 4: Visualization of the hairpin vortices.

Figure 5: Mean axial velocity profiles measured upstream of the first tab array.

$Re=10000$

Figure 6: Mean axial velocity profiles measured upstream and downstream of first and second tab arrays. $Re=10000$

Figure 7: Global view of evolution of mean axial velocity profile. $Re=10000$

Figure 8: Global view of evolution of mean axial velocity profile. $Re=1500$

Figure 9: Global view of evolution of mean axial velocity profile. $Re=3000$

Figure 10: Global view of evolution of turbulence intensity profile. $Re=10000$

Figure 11: Longitudinal evolution of turbulence intensity at 4 mm from the tube wall.

Triangles indicate locations of the tab arrays. $Re=10000$.

Figure 12: Effects of tab arrays on distribution of turbulence macro length scale.

$Re=10000$

Figure 13: Comparison of turbulence energy dissipation calculated with eq. 13 ($C=1$) and results of Lawn[1971]

Figure 14: Global evolution of turbulence energy dissipation profile. $Re=10000$

Figure 15: Temporal autocorrelation coefficient as a function of time for flow at the entrance to the mixer. $Re=15000$

Figure 16 : Temporal autocorrelation coefficient as a function of time downstream of the 7th tab array. $Re=15000$

Figure 17 : Variation of $\frac{\varepsilon_{\max}}{\varepsilon}$ along the static mixer

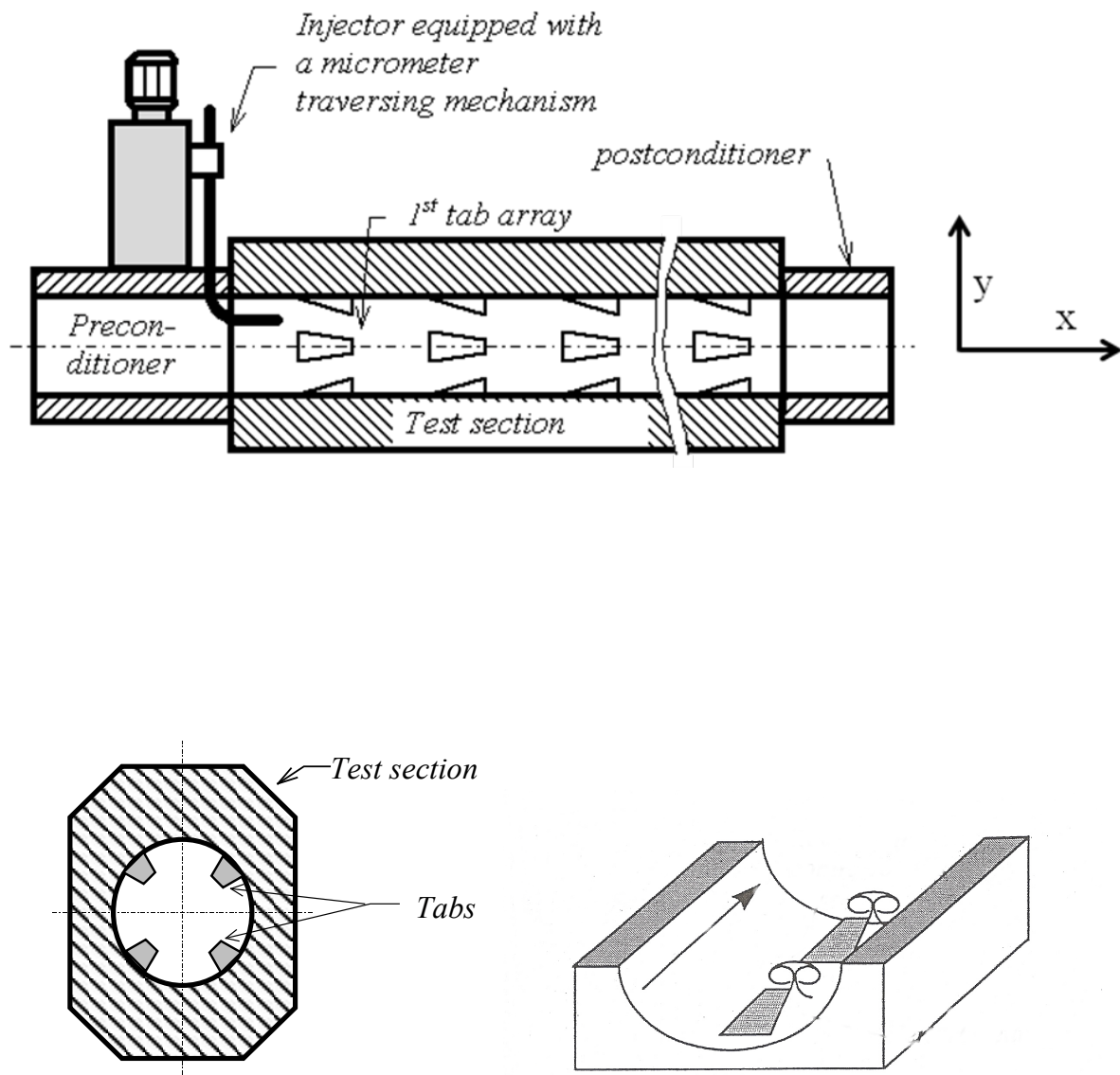


Figure 1 : Test section, preconditioner and postconditioner

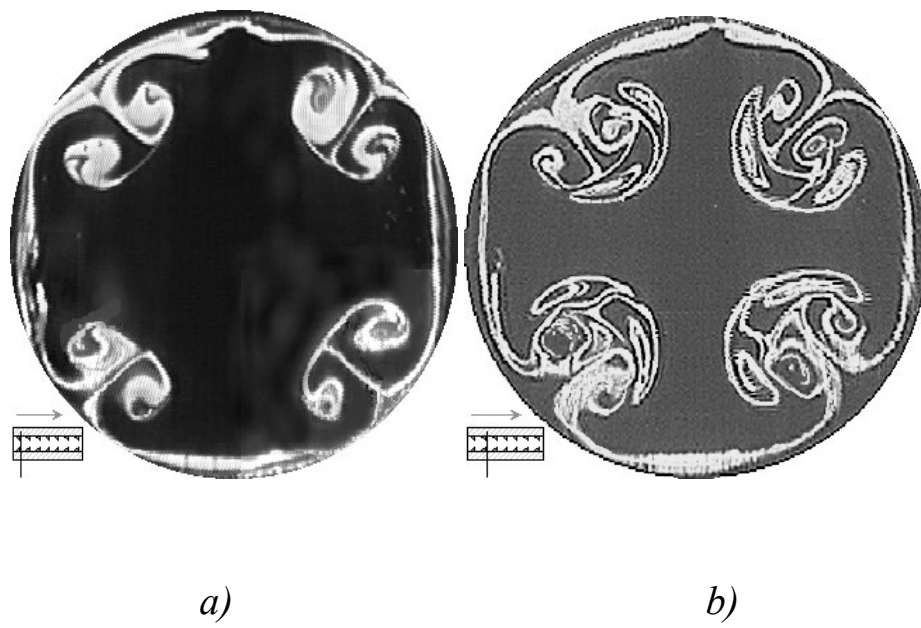


Figure2: Global flow visualization at two longitudinal positions. $Re=1000$.

a) 2 mm downstream first tab arrays b) 2 mm downstream second tab arrays.

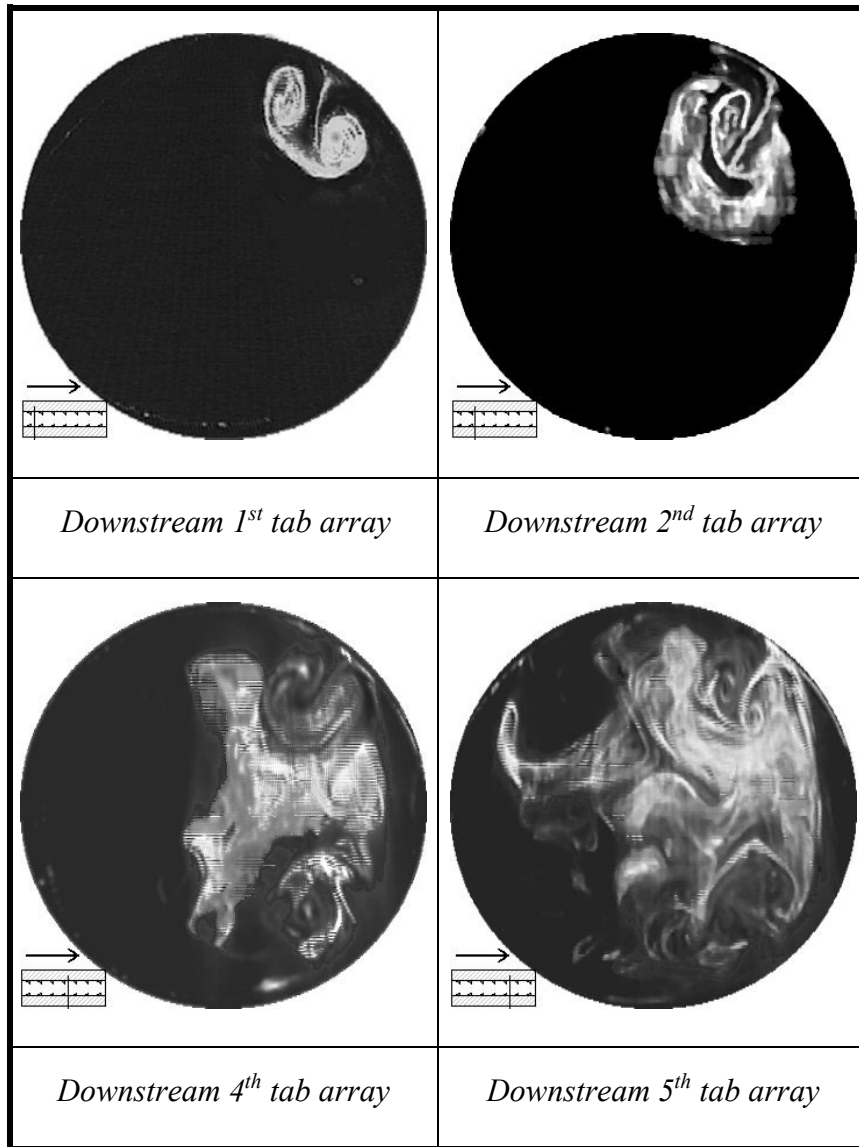


Figure 3: Photographs of the dye filament cross-section inside the static mixer

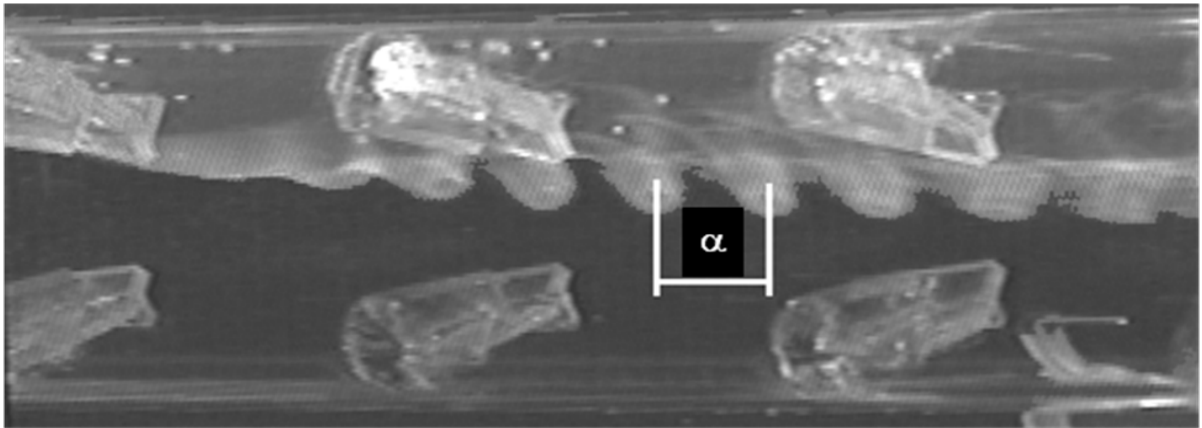


Figure 4: Visualization of the hairpin vortices.

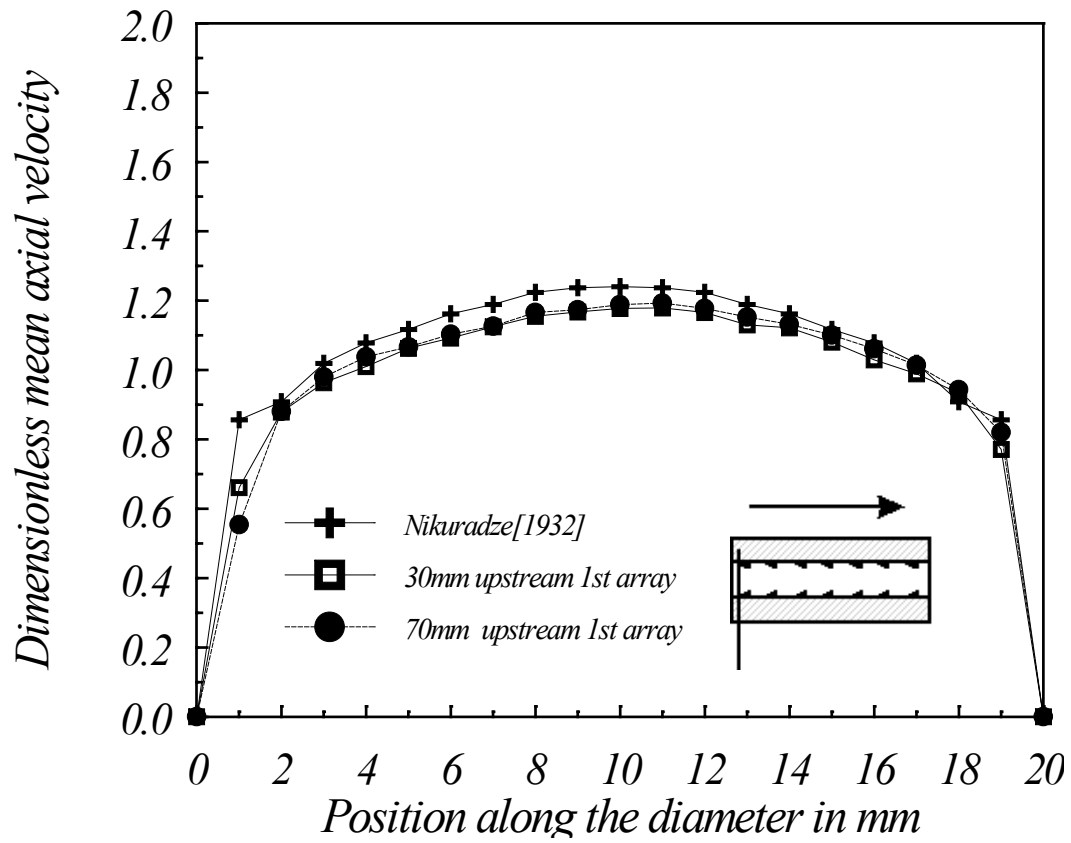


Figure5: Mean axial velocity profiles measured upstream of the first tab array. $Re=10000$

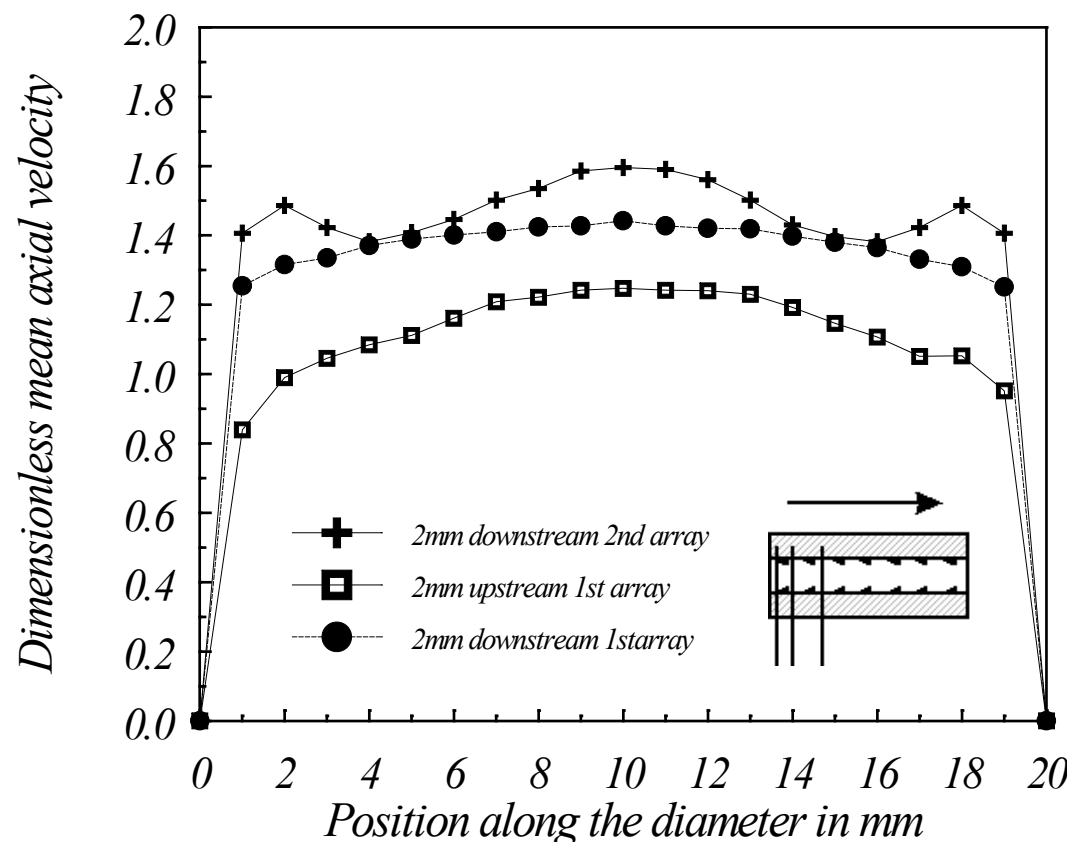


Figure 6: Mean axial velocity profiles measured upstream and downstream of first and second tab arrays. $Re=10000$

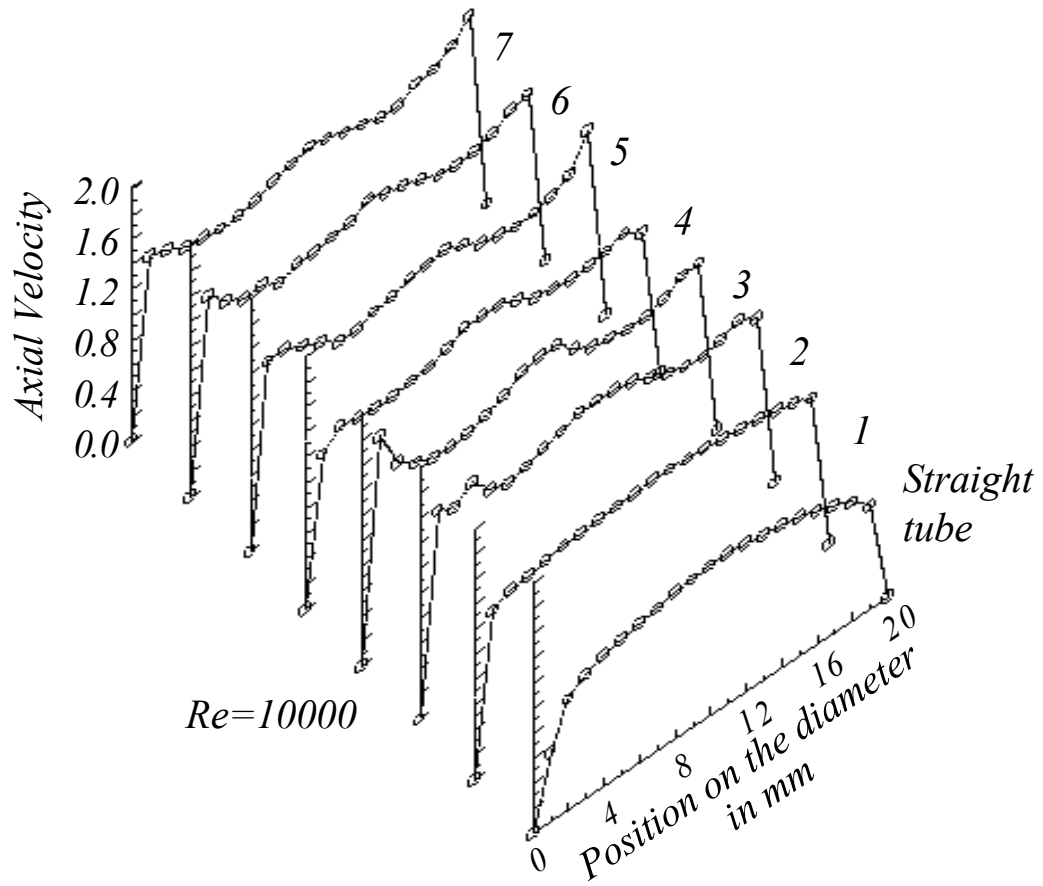


Figure 7: Global view of evolution of mean dimensionless axial velocity profile. $Re=10000$

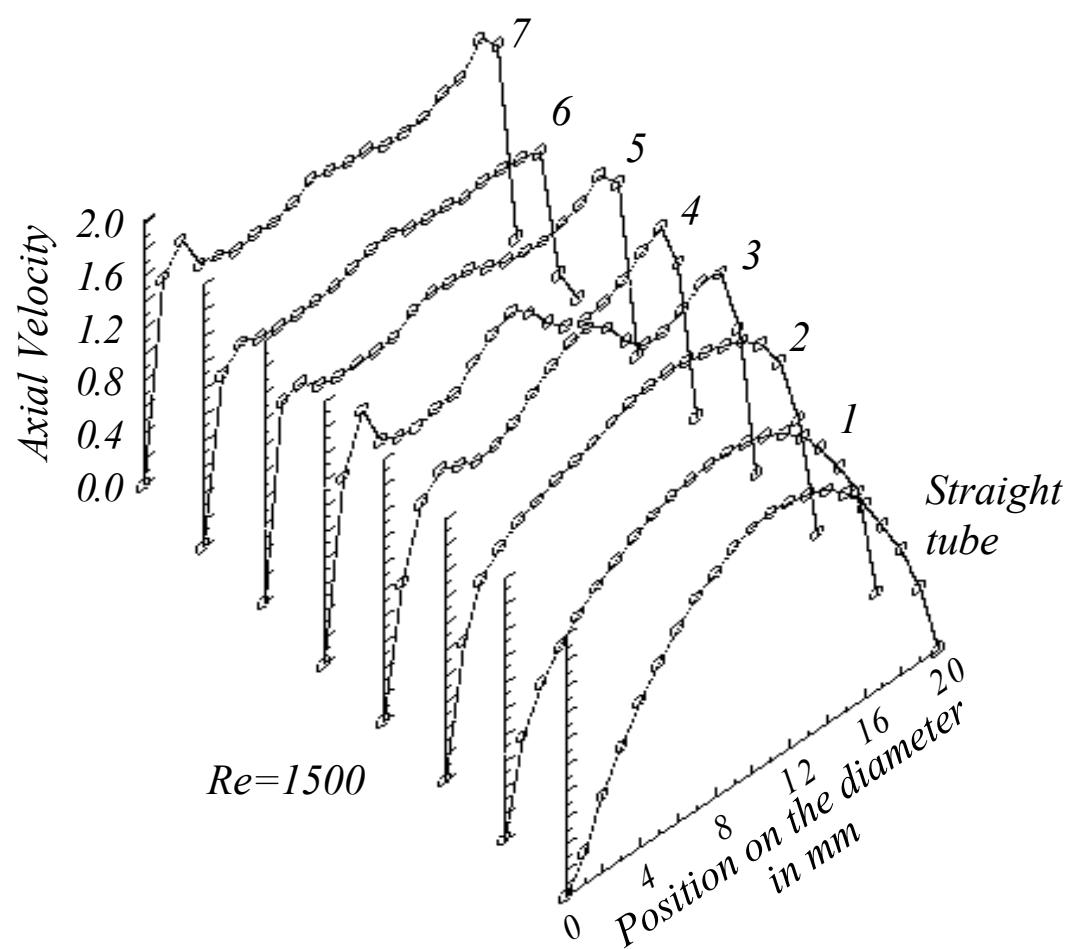


Figure 8: Global view of evolution of mean axial velocity profile. $Re=1500$

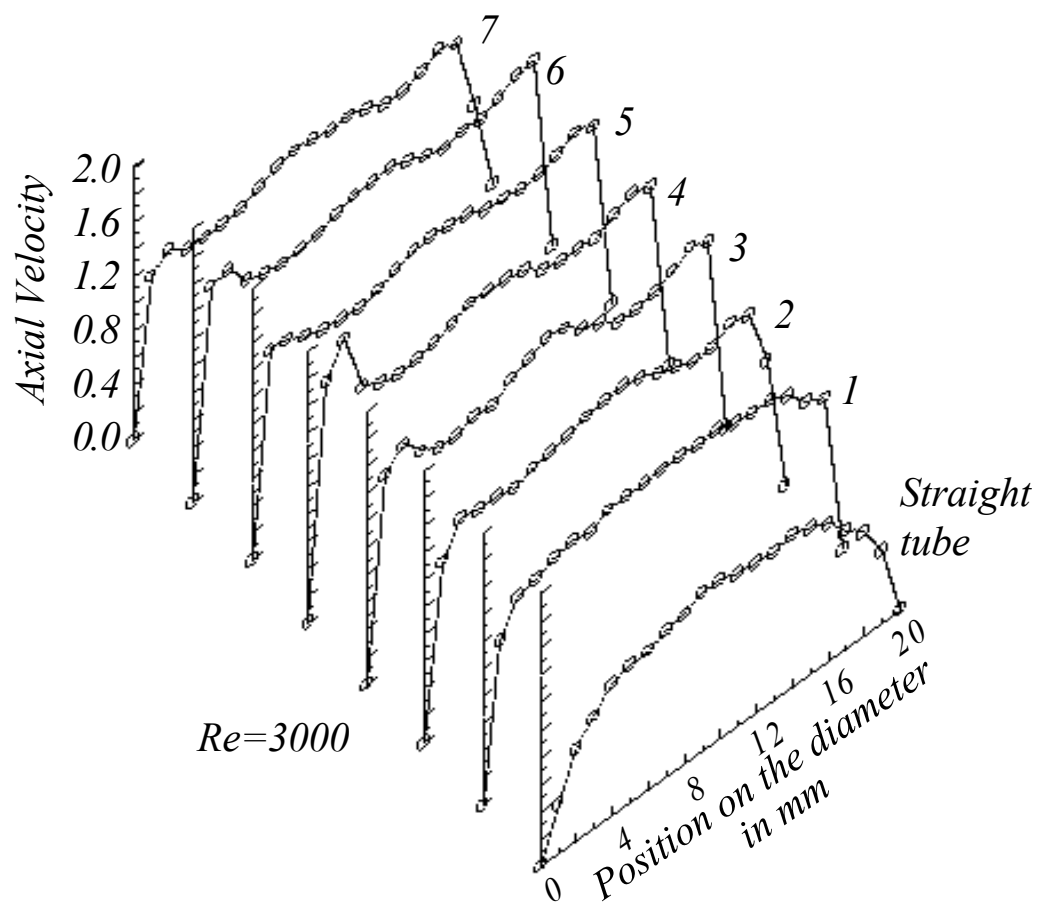


Figure 9: Global view of evolution of mean axial velocity profile. $Re=3000$

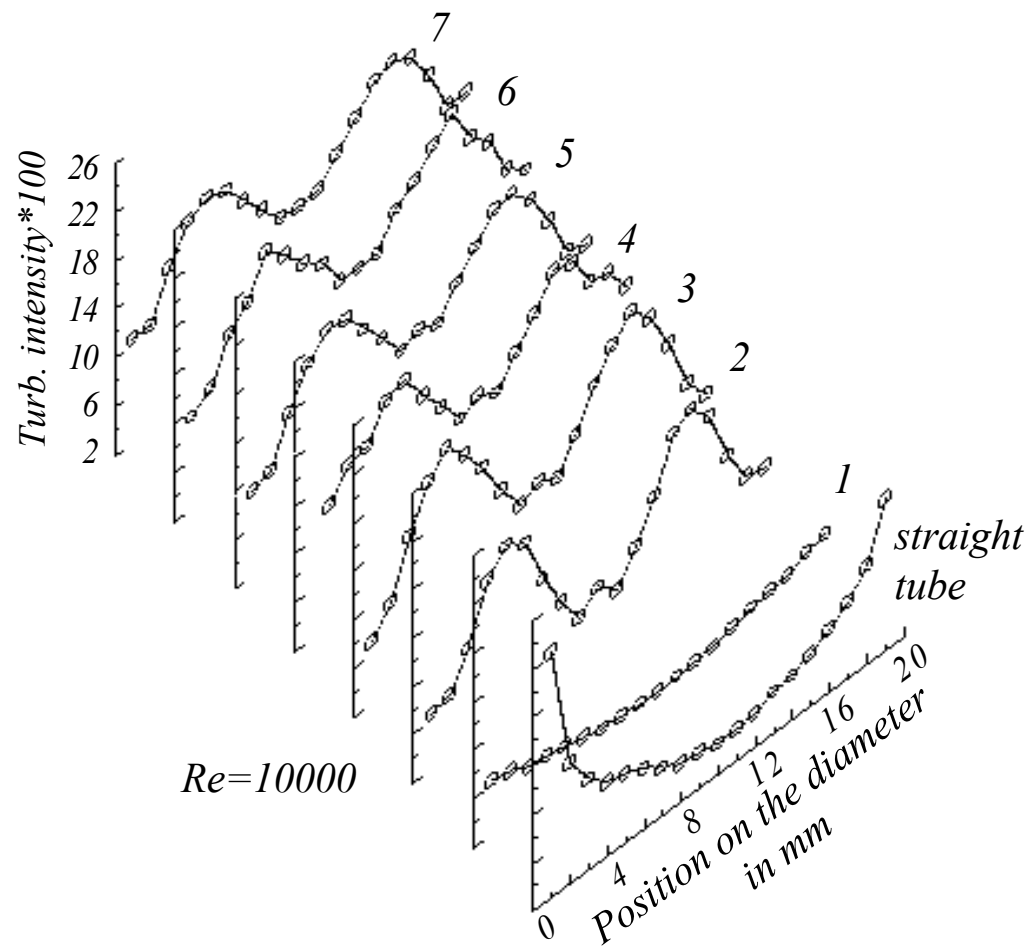


Figure 10: Global view of evolution of turbulence intensity profile. $Re=10000$

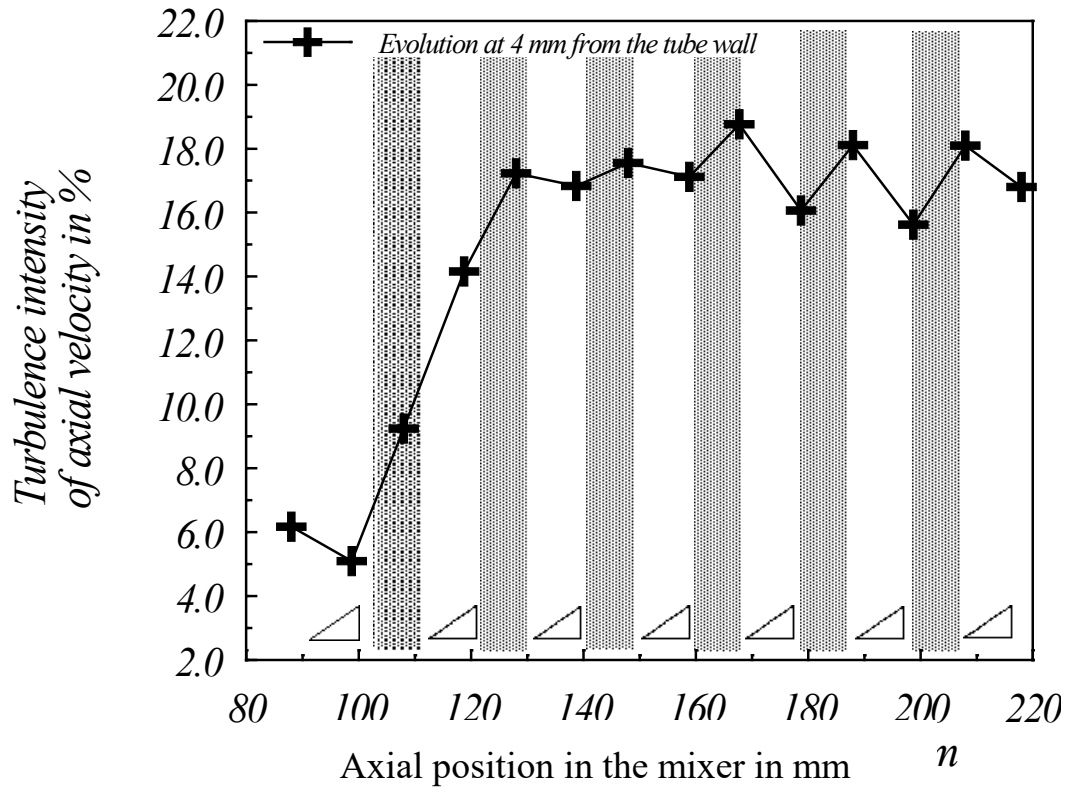


Figure 11: Longitudinal evolution of turbulence intensity at 4 mm from the tube wall.

Triangles indicate locations of the tab arrays. $Re=10000$.

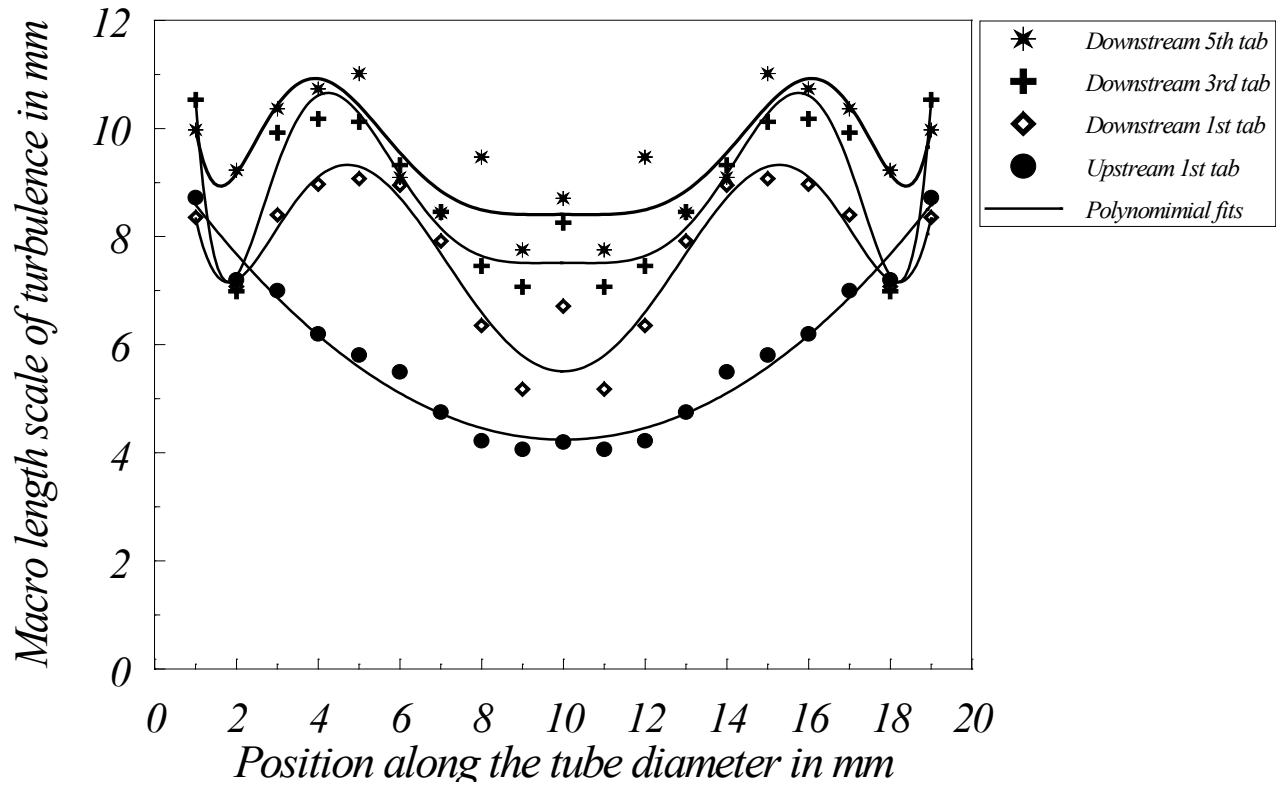


Figure 12: Effects of tab arrays on distribution of turbulence macro length scale.

Re=10000

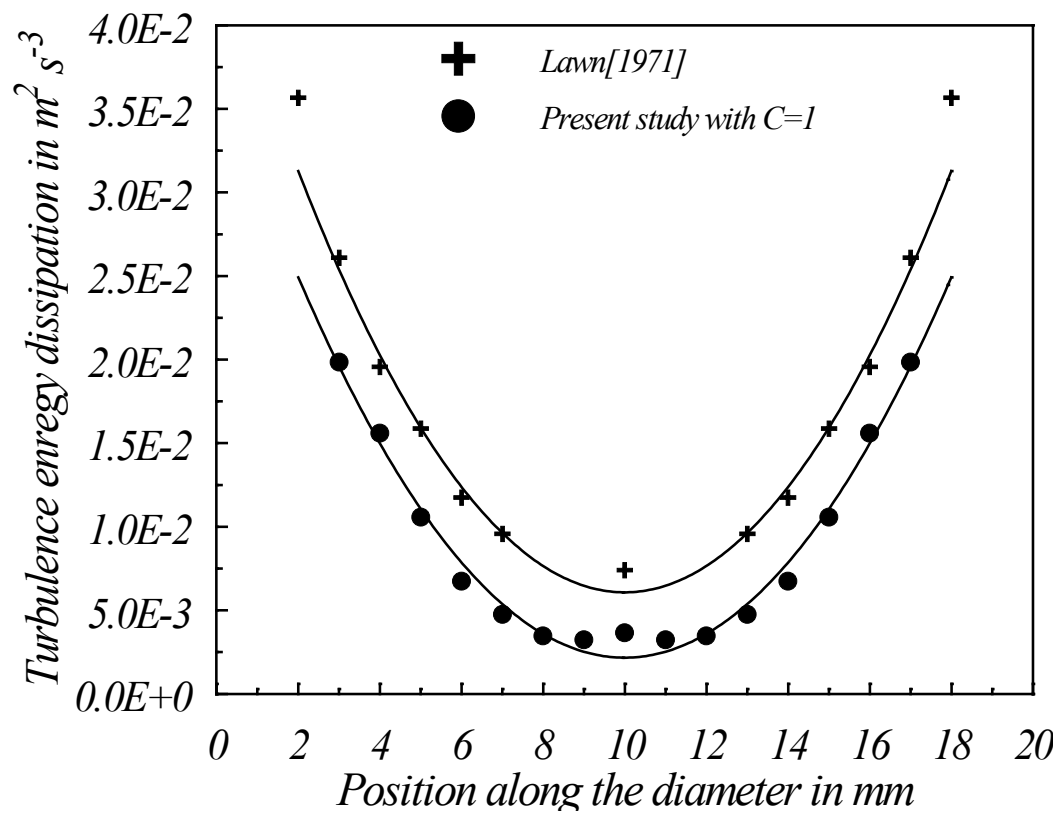


Figure 13: Comparison of turbulence energy dissipation calculated with eq. 13 (C=1) and results of Lawn[1971]

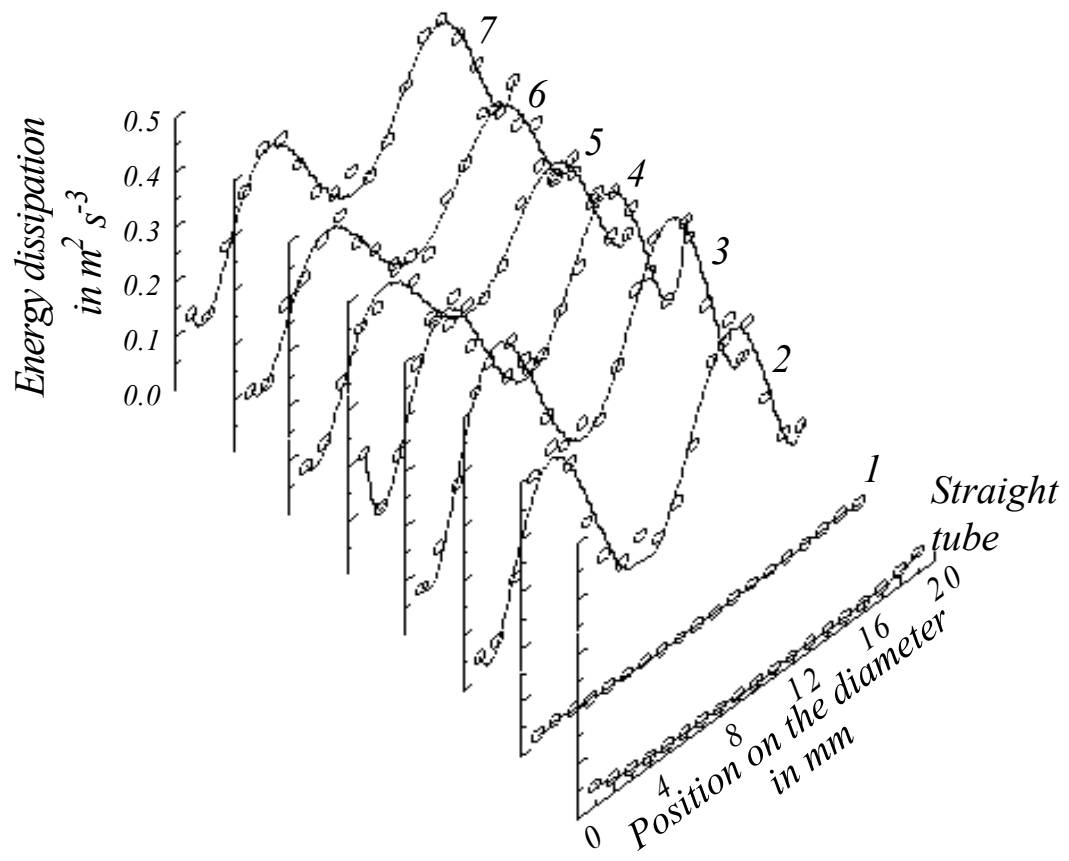


Figure 14: Global evolution of turbulence energy dissipation profile. $Re=10000$

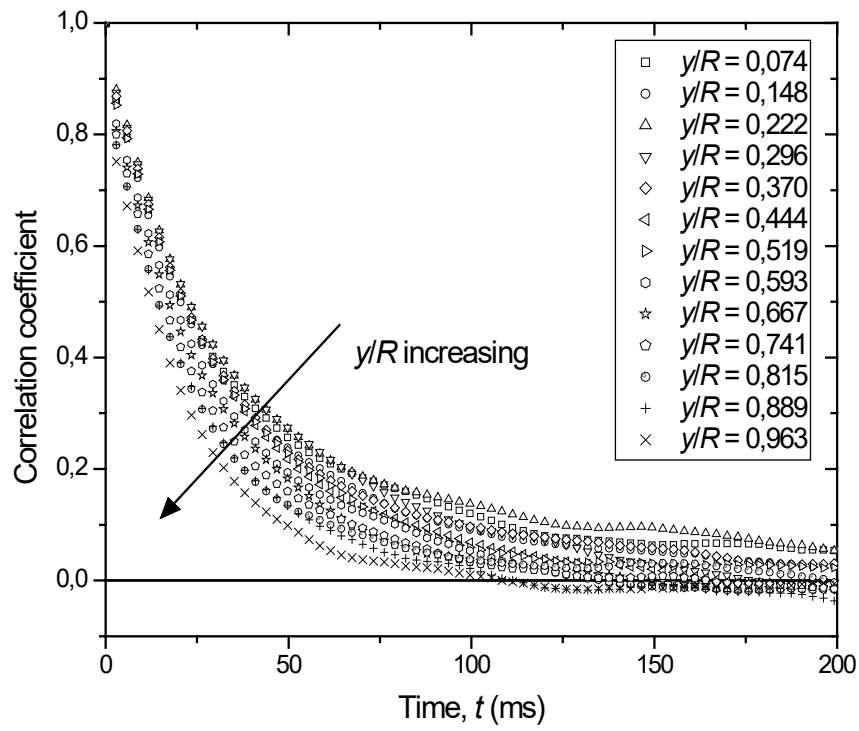


Figure 15: Temporal autocorrelation coefficient as a function of time for flow at the entrance to the mixer. $Re=15000$

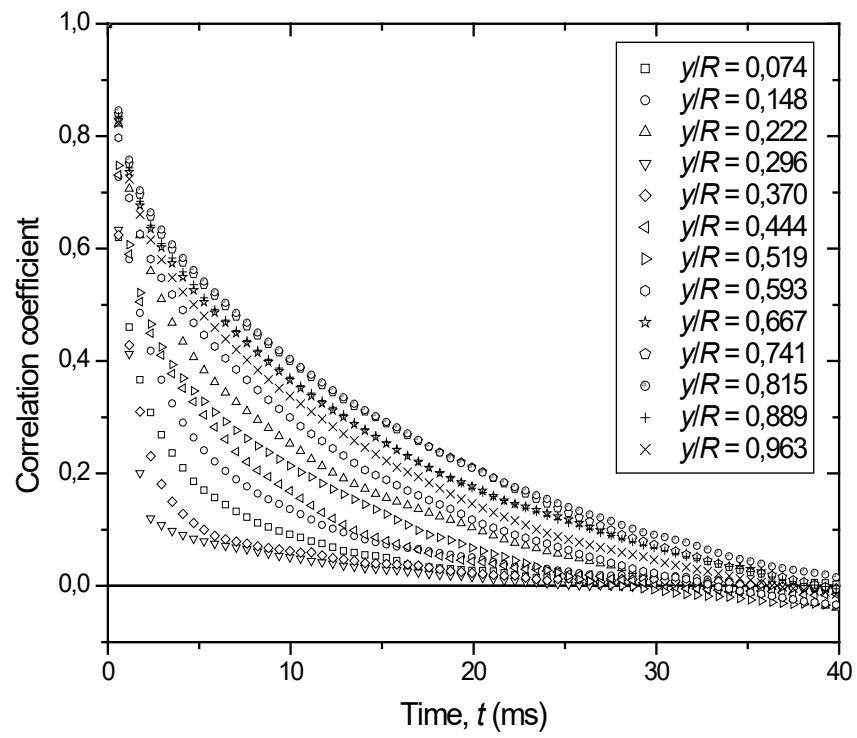


Figure 16 : Temporal autocorrelation coefficient as a function of time downstream of the 7th tab array. $Re=15000$

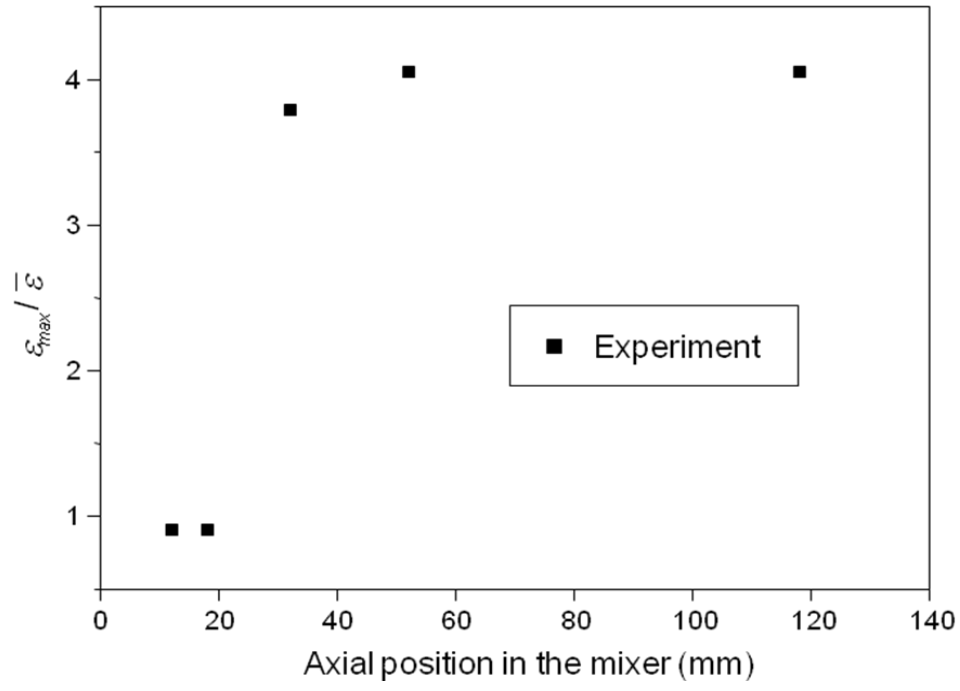


Figure 17: Variation of $\varepsilon_{\max} / \bar{\varepsilon}$ along the static mixer